Available online at www.sciencedirect.com

ScienceDirect

Journal of Otology 12 (2017) 9–17

www.journals.elsevier.com/journal-of-otology/

Clinically relevant human temporal bone measurements using novel high-resolution cone-beam CT

Jing Zou [a,b,*], Jaakko Lähelmä [c], Antti Arnisalo [d], Ilmari Pyykkö [b]

[a] Department of Otolaryngology-Head and Neck Surgery, Center for Otolaryngology-Head & Neck Surgery of Chinese PLA, Changhai Hospital, Second Military Medical University, Shanghai, China

[b] Hearing and Balance Research Unit, Field of Oto-laryngology, School of Medicine, University of Tampere, Tampere, Finland

[c] Planmeca Oy, Helsinki, Finland

[d] Department of Otorhinolaryngology-Head and Neck Surgery, Helsinki University Central Hospital, Helsinki, Finland

Received 16 December 2016; revised 12 January 2017; accepted 16 January 2017

Abstract

Objective: To test the feasibility of measuring fine temporal bone structures using a newly established cone-beam computed tomography (CBCT) system.

Materials and methods: Six formalin-fixed human cadaver temporal bones were imaged using a high-resolution CBCT system that has 900 frames and copper + aluminum filtration. Fine temporal bone structures, including those of the facial nerve canal and vestibular structures, were identified and measured.

Results: The fine structures of the middle ear, including the tympanic membrane, tendon of the tensor tympani, cochleariform process of the semicanal of the tensor tympani, pyramidal eminence, footplate of the stapes, full path of the facial nerve within the temporal bone, supralabyrinthine space, semicircular canals, pathway of the subarcuate canal, and full path of the vestibular aqueduct, were clearly demonstrated. The vestibular aqueduct has a midpoint width of 0.4 ± 0.0 mm and opercular width of 0.5 ± 0.1 mm (mean ± SD). The length of the internal acoustic meatus was 10.6 ± 1.2 mm (mean ± SD), and the diameter of the internal acoustic meatus was 3.7 ± 0.3 mm (mean ± SD).

Conclusion: This novel high-resolution CBCT system has potentially broad applications in the diagnosis of inner ear disease and in monitoring associated pathological changes, surgical planning, navigation for the ear surgery, and temporal bone training.

Keywords: CT; Temporal bone anatomy; Vestibule; Facial nerve

1. Background

Superior to multi-detector computed tomography (MDCT), cone-beam CT (CBCT) has fast data acquisition (less than a minute versus several minutes for MDCT), low-dose exposure of the subject, smaller floor area footprint of the imaging apparatus, a relatively low equipment purchase price, and has broad applications in head and neck imaging (Stutzki et al., 2015). The excellence of CBCT in temporal bone imaging has been demonstrated including visualization of the intrascalar positions of cochlear implant electrodes and facial nerve canal measurements and potential diagnosing semicircular canal dehiscence (Eibenberger et al., 2014; Husstedt et al., 2002; Komori et al., 2013; Pearl et al., 2014; Verbist et al., 2005; Zou et al., 2015b). Even a prototype system for intraoperative CBCT imaging has been developed to track the drill during temporal bone surgery (Erovic et al., 2013).

* Corresponding author. Department of Otolaryngology-Head and Neck Surgery, Changhai Hospital, Second Military Medical University, Changhai Road #168, Shanghai, 200433, China.

E-mail addresses: zoujinghb@hotmail.com, Jing.Zou@uta.fi (J. Zou).

Peer review under responsibility of PLA General Hospital Department of Otolaryngology Head and Neck Surgery.

http://dx.doi.org/10.1016/j.joto.2017.01.002

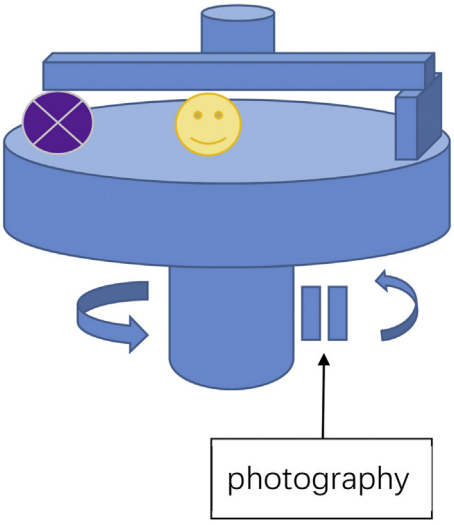

Fig. 1. Illustration of the novel CBCT system. The system is composed of an imaging part on the top and a mechanic plateform at the bottom. The spaceman was placed on the plateform that rotates. A pause (‖) was included in the rotation during each exposure for photography.

For both diagnosing the middle and inner ear diseases and intraoperative tracking of the drill during temporal bone surgery, it is necessary to obtain images with high spatial resolution. Bremke et al. reported visualization of experimental superior semicircular canal dehiscence (SSCD) using a CBCT with voxel resolution (section thickness) of 0.125 mm (Bremke et al., 2015). Although CBCT was significantly better than MDCT in identifying a thin bony coverage of a superior semicircular canal (SSC), the reliability of the radiological findings does not legitimate the diagnosis of an SSCD based on radiologic data alone due to existence of false-positive results. There is still a room to improve the resolution of CBCT. We recently designed a novel high-resolution CBCT acquisition system with voxel size of 0.1 mm that involves a pause during each of the exposures of the multiple frames (Fig. 1) (Zou et al., 2015a). The new CBCT system provided a chance to improve the accuracy of diagnosis and intraoperative tracking of the drill. Aimed to test the feasibility in clinical use, we analyzed the critical temporal bone structures, including the vestibular aqueduct, the semicircular canal wall, the facial

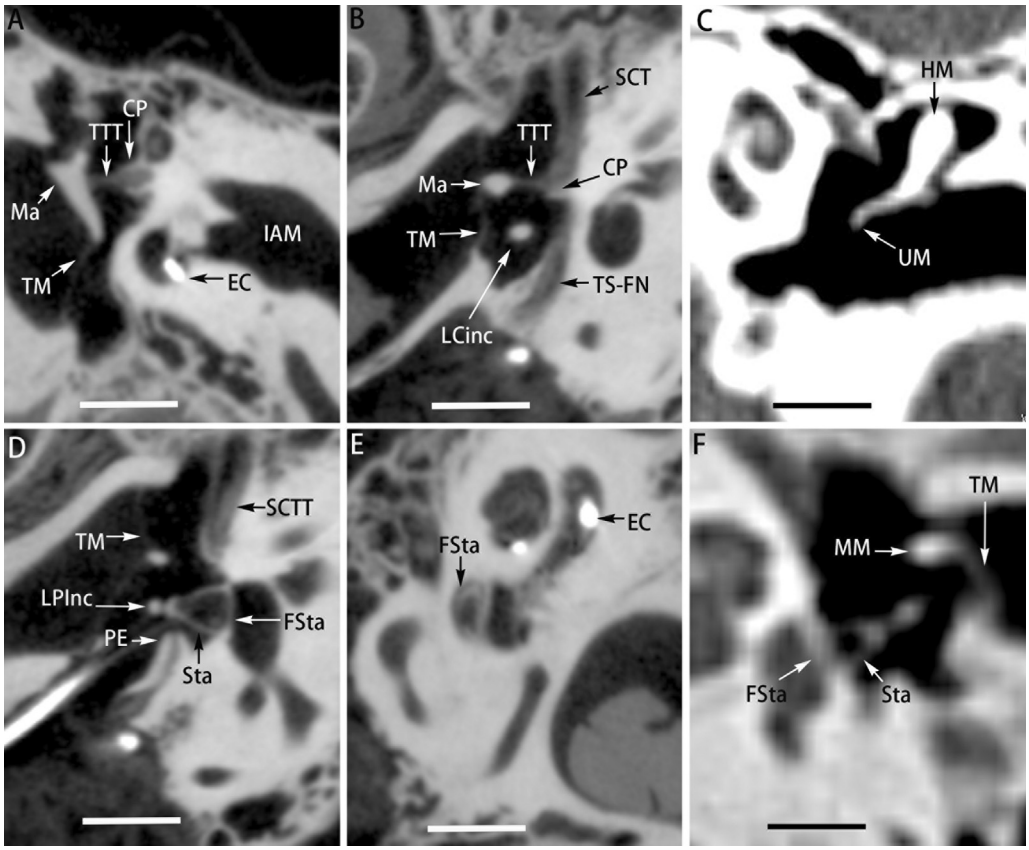

Fig. 2. Middle ear structures of the temporal bone demonstrated by a novel high-resolution CBCT system in comparison to the conventional MDCT. In CBCT, a total of 900 cone-beam projections were acquired by rotating the specimen (left side A, B, and D; right side E) around axial axis and the target structures were identified by adjusting the location and orientation of the axial, sagittal and coronal viewing planes. In MDCT, the isotropic volumes of entire temporal bone including both sides were acquired on axial orientation. The target structures were displayed by adjusting the location and orientation of the axial, sagittal and coronal viewing planes of the selected the left side (C, F). CP: cochleariform process; EC: electrode contact; EEC: external ear canal; Sta: stapes; FSta: footplate of the stapes; HM; head of malleus; IAM: internal auditory meatus; Ma: malleus; MM: manubrium of malleus; TTT: tendon of the tensor tympani; SCTT: semicanal of the tensor tympani; LPInc: lenticular process of the incus; LCInc: long crus of the incus; PE: pyramidal eminence; TM: tympanic membrane; TS-FN: tympanic segment of the facial nerve; UM: umbo of malleus. Scale bar = 5 mm.

nerve canal and the internal meatus, using the newly established CBCT system.

2. Materials and methods

2.1. CBCT imaging

Six formalin-fixed human cadaver temporal bones from deceased Finnish patients were used in the study. All specimens were donated to the University of Tampere for scientific use and fulfilled all requirements of the Declaration of Helsinki, which was developed by the World Medical Association and updated at the 64th WMA General Assembly in Fortaleza, Brazil, in 2013 regarding the ethical use of human materials (World Medical Association, Inc., 2015). These temporal bones were operated on for cochlear implant electrode insertion in a previous study (Zou et al., 2015a, 2015b). The imaging parameters selected for the present study included the following: number of frames, 900; tube voltage, 88 kV; tube current, 11 mA; exposure length per frame, 50 ms; filtration, 0.5 mm copper + 2.5 mm aluminum; source-to-image distance, 1 m; magnification factor, 1.72; voxel size, 0.1 mm; and field of view (FOV), 60 × 60 mm. These parameters were previously optimized (Zou et al., 2015a).

2.2. Image processing

The captured X-ray exposure frames were reconstructed using the filtered backprojection algorithm. Gamma correction was applied to the reconstructed images and the processed images were visualized using the Romexis software version 3.0 (Planmeca Oy, Helsinki, Finland). The fine temporal bone structures, including the facial nerve canal and the vestibular structures, were identified by adjusting the location and orientation of the axial, sagittal and coronal viewing planes. The vestibular aqueduct was confirmed by following its origin in the vestibule. The supralabyrinth space was evaluated and specifically the course of the subarcuate canal was followed from the subarcuate fossa in the posterior cranial fossa to the mastoid antrum. The wall thickness of the semicircular canal at the thinnest site, the width of vestibular aqueduct at midpoint and opercular point, the diameter of the facial nerve canal at the narrowest site in the labyrinthine segment, and the diameter and length of the internal acoustic meatus were measured using the above-referenced software.

2.3. MDCT imaging

Toshiba (Aquilion ONE™, Toshiba Medical Systems Corporation, Tokyo, Japan) with 320-row detector was used to acquire isotropic volumes of entire temporal bone including both sides in a patient suspected of vestibular paroxysmia on axial orientation. The following parameters were used: voltage 135 kV, current 400 mA, FOV 24.0 cm, slice thickness 0.412 mm, magnification factor 1.00, and matrix 512 × 512. The desired structures were demonstrated using multiplanar mode.

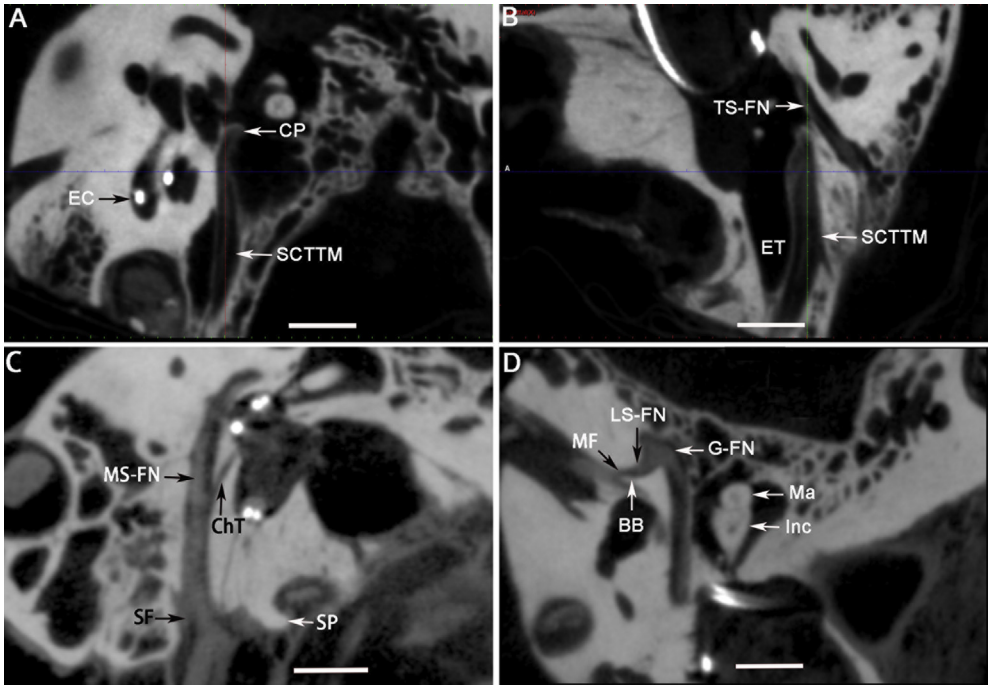

Fig. 3. Important landmarks of the facial nerve canal in the temporal bone shown by a novel high-resolution CBCT system. The target structures were identified by adjusting the location and orientation of the axial, sagittal and coronal viewing planes of cone-beam projections on axial axis of a left temporal bone (A–D). BB: Bill's bar; ChT: chorda tympani; CP: cochleariform process; EC: electrode contact; ET: Eustachian tube; G-FN: geniculum of the facial nerve; Inc: incus; LS-FN: labyrinth segment of the facial nerve; Ma: malleus; MF: meatus foramen; MS-FN: mastoid segment of the facial nerve; SCTTM: semicanal of the tensor tympani muscle; SF: stylomastoid foramen; SP: styloid process; TS-FN: tympanic segment of the facial nerve. Scale bar = 5 mm.

2.4. Statistics

The mean values and standard deviation (SD) of the measures were calculated.

3. Results

High-quality temporal bone images were acquired using the novel CBCT set-up in combination with the optimized imaging parameters. In addition to the ossicular chain, the fine structures of the middle ear, including the tympanic membrane, the tendon of the tensor tympani, the cochleariform process of the semicanal of the tensor tympani, the pyramidal eminence, and the footplate of the stapes, were clearly demonstrated (Fig. 2). Although the MDCT clearly displayed the ossicular chain and the fine architectures of stapes, the resolution was significantly lower than that acquired using the current CBCT system (Fig. 2). The labyrinthine, tympanic, and mastoid segments of the facial nerve were demonstrated with high resolution (Fig. 3). The cochleariform process of the tensor tympani was always identified as a landmark to locate the starting point of the tympanic segment of the facial nerve (Fig. 4). The shortest distance between the cochleariform process and the tympanic segment of the facial nerve was 0.5 ± 0.2 mm (mean ± SD) (Table 1). The greater superficial petrosal nerve that originates from the geniculum of the facial nerve was also identified (Fig. 5). The narrowest site of the meatal foramen measured 0.9 ± 0.3 mm (mean ± SD, Table 1). The semicircular canals were illustrated with high accuracy, and the supralabyrinthine space was clearly demonstrated (Fig. 6). Among the supralabyrinthine space (air cell tract), posterosuperior, posteromedial, subarcuate, and anterior tracts were visualized in several temporal bones. The posteromedial and subarcuate tracts were detected in all the 6 temporal bones. The posterosuperior tracts appeared in 5/6 temporal bones. The anterior supralabyrinthine tracts were identified in 2/6 temporal bones. The posterior semicircular wall exhibited the greatest variability with respect to thickness. The lateral semicircular canal wall was the thinnest followed by the superior semicircular canal wall, while the posterior semicircular canal wall was the thickest (Table 1). The pathway of the subarcuate canal was also delineated by the subarcuate fossa to the mastoid antrum, and the accompanying subarcuate air cells were easily distinguished from the subarcuate (Fig. 7). The vestibular aqueduct, which is the finest canal in the temporal bone, was followed from the origin in the utricle and saccule to the opening in the posterior fossa (opercular point), which hosts the endolymphatic sac (Fig. 8). The vestibular aqueduct has a midpoint width of 0.4 ± 0.0 mm and opercular width of 0.5 ± 0.1 mm (mean ± SD, Table 1). The length of the internal acoustic meatus exhibited the greatest variability among all of the critical measures of the temporal bone, and its value was 10.6 ± 1.2 mm (mean ± SD), while the diameter of the internal acoustic meatus exhibited a smaller variability and a value of 3.7 ± 0.3 mm (mean ± SD, Fig. 9, Table 1).

Table 1
Measures of the critical structures of the human temporal bones using the novel CBCT system.

Structures	n	Mean (mm)	SD
IAM-D	6	3.7	0.3
IAM-L	6	10.6	1.2
FNMF-D	6	0.9	0.3
FNCP-D	6	0.5	0.2
SSCC-W	6	0.8	0.1
PSCC-W	6	1.9	0.6
LSCC-W	6	0.7	0.1
VAM	6	0.4	0.0
VAO	6	0.5	0.1

IAM-D: diameter of the internal acoustic meatus; IAM-L: length of internal acoustic meatus; FNMF-D: diameter of the facial nerve canal at the site of the meatal foramen; SSCC-W: wall of the superior semicircular canal; PSCC-W: wall of the posterior semicircular canal; LSCC-W: wall of the lateral semicircular canal; VAM: vestibular aqueduct midpoint; VAO: vestibular aqueduct operculum; FNCP-D: distance between the cochleariform process and tympanic segment of the facial nerve.

4. Discussion

The present work demonstrated that a novel high-resolution CBCT system was able to illustrate the fine anatomy of human temporal bones. Regarding the facial nerve, the full course within the temporal bone was visualized, and all of the critical landmarks were consistently identified. Visualization of the meatus foramen and geniculum of the facial nerve is relevant for the diagnosis of Bell's palsy and helpful for the

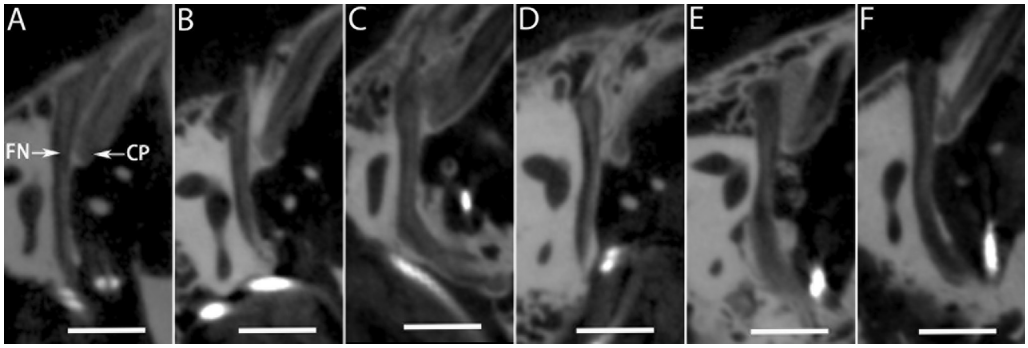

Fig. 4. Spatial association between the cochleariform process and the tympanic segment of the facial nerve demonstrated by the novel high-resolution CBCT system. The target structures were identified by adjusting the location and orientation of the axial, sagittal and coronal viewing planes of cone-beam projections on axial axis of either left (A, B, C, and E) or right (D, F) temporal bones. CP: cochleariform process; FN: facial nerve. Scale bar = 5 mm.

corresponding surgical procedure (Murai et al., 2013). Visualizations of the fine structures of the greater superficial petrosal nerve and the tensor tympani are relevant to surgical design for facial nerve decompression. The greater superficial petrosal nerve is a landmark for the identification of the geniculum of the facial nerve, which is the most frequent site of fracture in cases of temporal bone trauma causing facial palsy (Rajati et al., 2014). The tensor tympani approach with

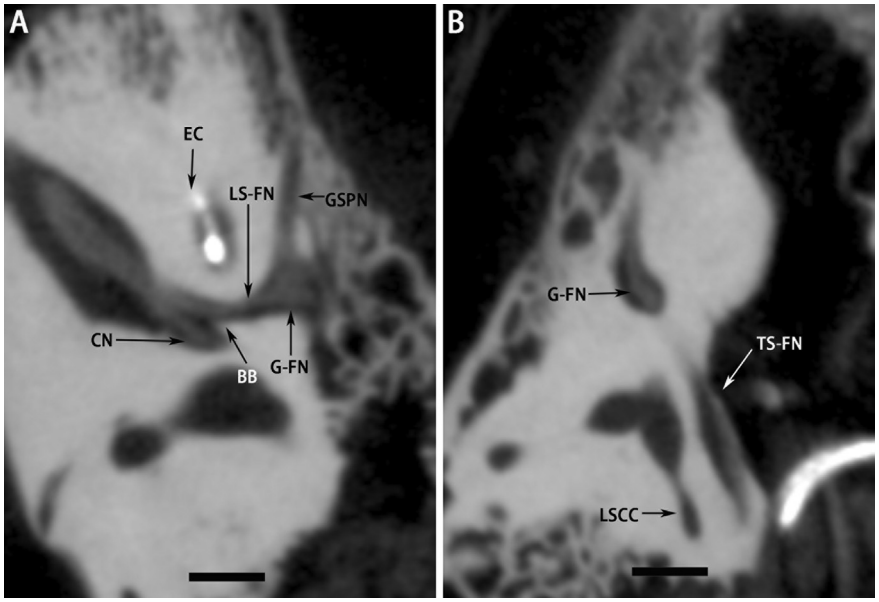

Fig. 5. Greater superficial petrosal nerve demonstrated by the novel high-resolution CBCT system. The target structures were identified by adjusting the location and orientation of the axial, sagittal and coronal viewing planes of cone-beam projections on axial axis of a right temporal bone (A, B). BB: Bill's bar; CN: cochlear nerve; EC: electrode contact; G-FN: geniculum of the facial nerve; GSPN: greater superficial petrosal nerve; LSCC: lateral semicircular canal; LS-FN: labyrinth segment of the facial nerve; TS-FN: tympanic segment of the facial nerve. Scale bar = 3 mm.

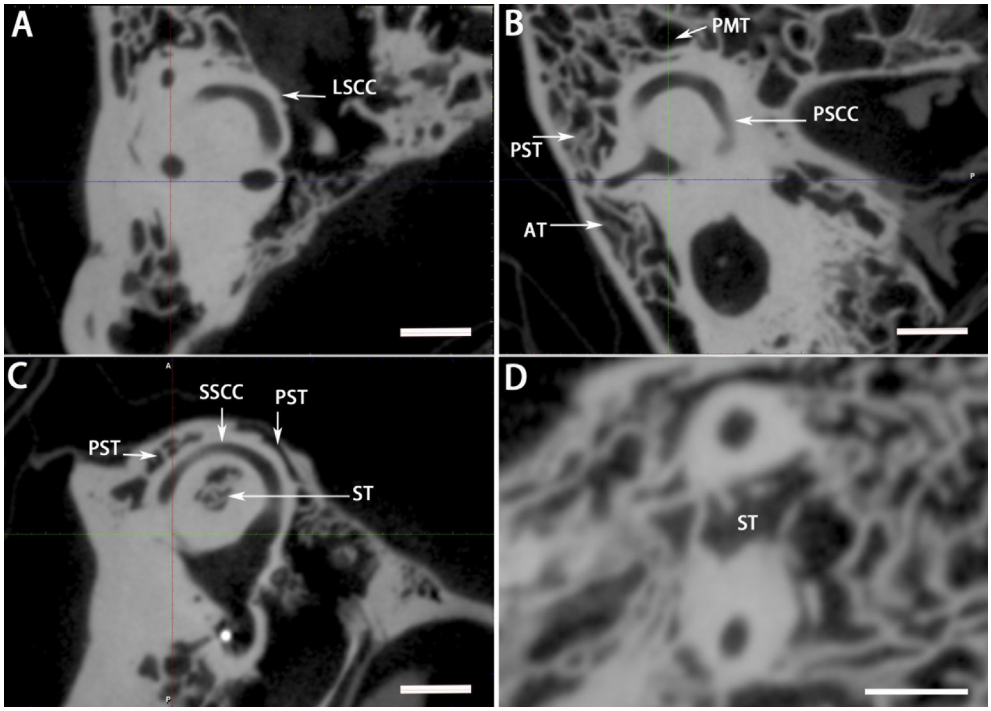

Fig. 6. Semicircular canals and supralabyrinthine space demonstrated by CBCT. The target structures were identified by adjusting the location and orientation of the axial, sagittal and coronal viewing planes of cone-beam projections on axial axis of a left temporal bone (A–D). AT: anterior tract of supralabyrinthine space; LSCC: lateral semicircular canal; PMT: posteromedial tract of supralabyrinthine space; PST: posterosuperior supralabyrinthine space; PSCC: posterior semicircular canal; ST: subarcuate tract of supralabyrinthine space; SSCC: superior semicircular canal. Scale bar = 5 mm.

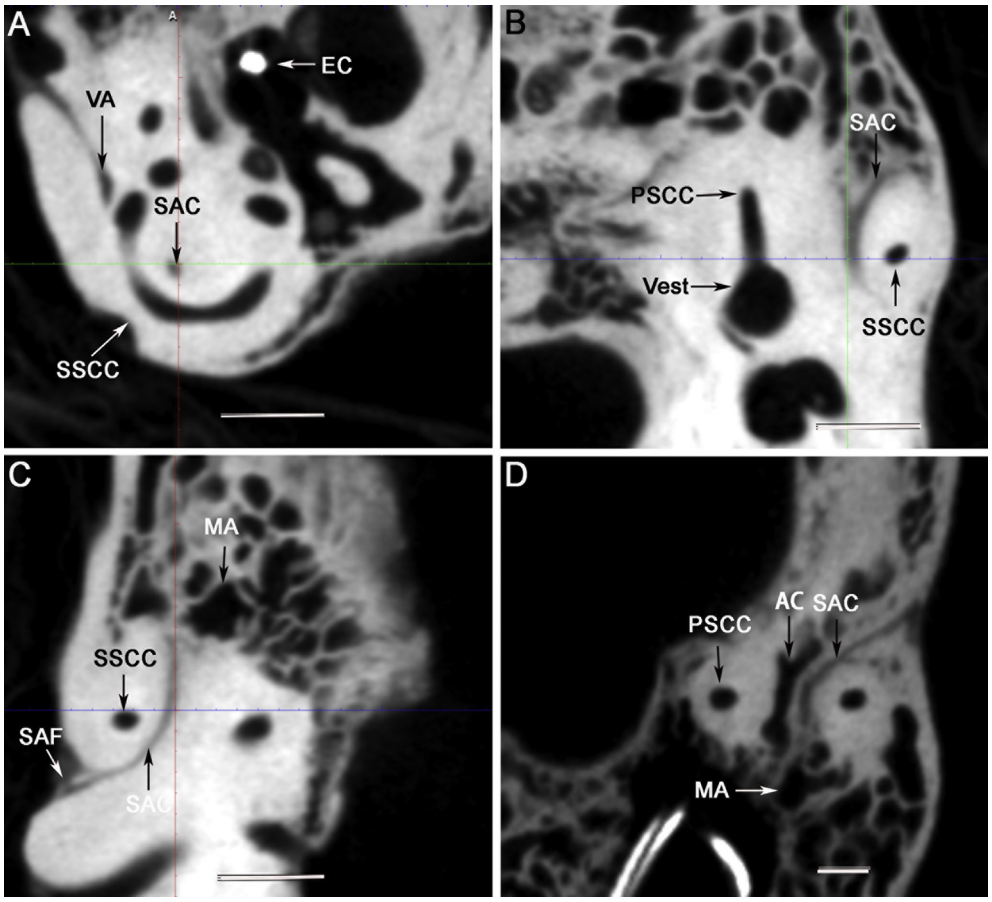

Fig. 7. Subarcuate canal demonstrated by the novel high-resolution CBCT system. The target structures were identified by adjusting the location and orientation of the axial, sagittal and coronal viewing planes of cone-beam projections on axial axis of either left (D) or right (A–C) temporal bones. AC: air cell; EC: electrode contact; MA: mastoid antrum; PSCC: posterior semicircular canal; SAC: subarcuate canal; SAF: subarcuate fossa; SSCC: superior semicircular canal; VA: vestibular aqueduct; Vest: vestibule. Scale bar = 5 mm.

extended posterior tympanotomy can even be used to remove bony fragments at the base of the geniculate ganglion (Jung et al., 2013).

Using the novel high-resolution CBCT system, all of the semicircular canals were clearly visualized, and accurate measures were obtained. The posterior semicircular canal has the thickest wall among the semicircular canals. The full course of the subarcuate canal from the subarcuate fossa to the mastoid antrum was visualized, and the accompanying subarcuate air cells were distinguished from the subarcuate canal. It has been reported that subarcuate venous malformations cause audio-vestibular symptoms similar to those of SCCD (Brantberg et al., 2004). The sufficient demonstration of the full course of the vestibular aqueduct using the novel high-resolution CBCT provides a useful tool for the diagnosis of enlarged vestibular aqueduct (EVA). EVA can be confirmed by either CT or magnetic resonance imaging (MRI), and the former is most commonly used in the clinic because other inner ear malformations can be detected by CT with high efficacy. It has been reported that 45% of patients with EVA have vestibular signs and symptoms (Zalewski et al., 2015). There is an urgent need to use CBCT to detect EVA in the clinic because this condition occurs in children who are extremely sensitive to the radiation created by CT imaging. Superior semicircular canal dehiscence (SSCD) was first described in a report from Minor et al., in 1998 based on CT imaging (Minor et al., 1998). In 2007, Zhou et al. reported a case of SSCD in a young child at the age of 12 years and suggested that SSCD is a developmental defect. The co-existence of SSCD and EVA further supported this developmental hypothesis (Ma et al., 2009; Zhou et al., 2007). The present study revealed that the average width of vestibular aqueduct is 0.4 at midpoint and 0.5 at opercular site, which is far below the value for EVA (Boston et al., 2007). This novel system may also provide additional information to aid the understanding of the congenital etiology of Meniere's disease in association with malformations of the vestibular aqueduct. Information about the vestibular aqueduct malformation in Meniere's disease has been obtained using CBCT imaging (Yamane et al., 2015). Accurate measures of the vestibular aqueduct using our high-resolution CBCT will provide a reliable tool for investigations of the potential pathological changes in Meniere's disease.

The supralabyrinthine space was detected using MDCT and has clinical significance in the temporal bone drilling and exploration of the medial wall of the attic for cholesteatoma

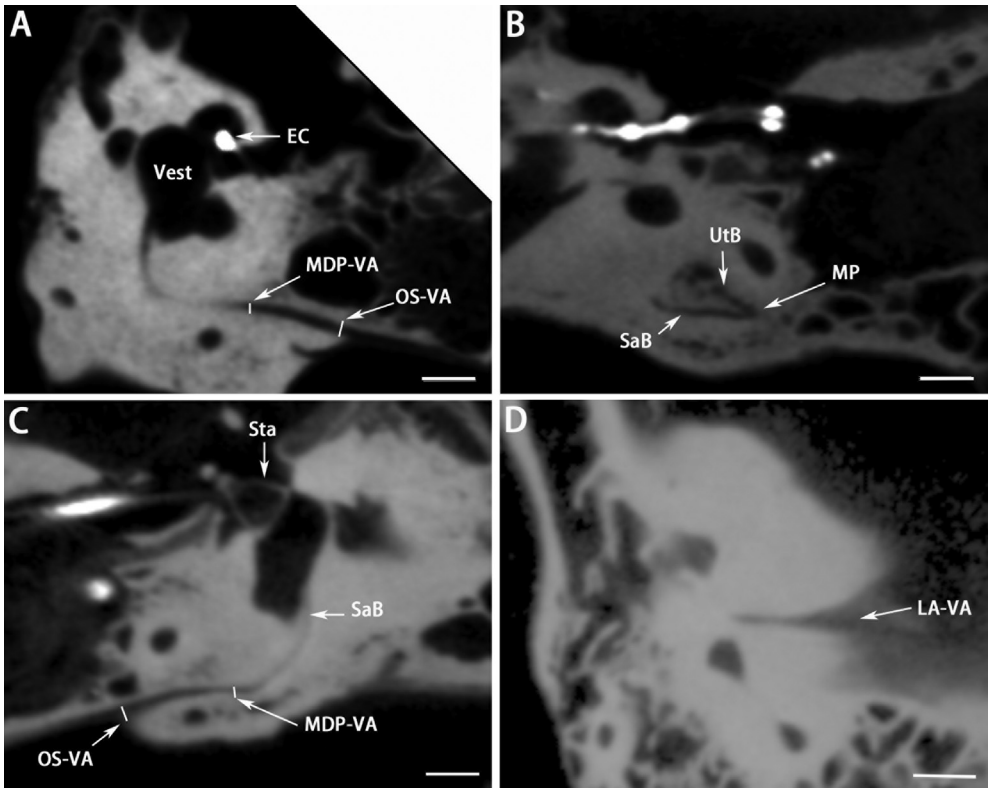

Fig. 8. Pathway of the vestibular aqueduct demonstrated by the novel high-resolution CBCT system. The target structures were identified by adjusting the location and orientation of the axial, sagittal and coronal viewing planes of cone-beam projections on axial axis of either left (A–C) or right (D) temporal bones. EC: electrode contact; LA–VA: Longitudinal axis of external aperture of the vestibular aqueduct; MDP-VA: midpoint of vestibular aqueduct; MP: meeting point of the vestibular aqueduct; OS-VA: opercular site of vestibular aqueduct; SaB: saccular branch of the vestibular aqueduct; Sta: stapes; UtB: utricular branch of the vestibular aqueduct; VA: vestibular aqueduct; Vest: vestibule. Scale bar = 5 mm.

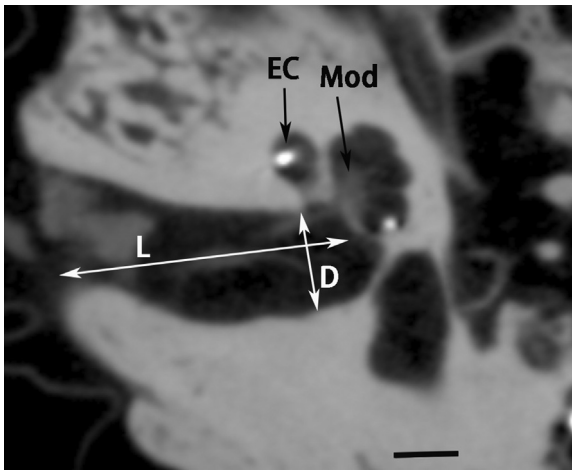

Fig. 9. Measurement of the internal acoustic meatus on the CBCT image. The target structures were identified by adjusting the location and orientation of the axial, sagittal and coronal viewing planes of cone-beam projections on axial axis of a left temporal bone. EC: electrode contact; D: diameter; L: length; Mod: modiolus. Scale bar = 5 mm.

removal and facial nerve decompression (Gluth et al., 2011; Jiang et al., 2012; Ni et al., 2016; Yamakami et al., 2003). CBCT showed excellent performance in detecting this region and revealed that the anterior supralabyrinthine air cells appeared infrequently in the temporal bones comparing to the other air cells of the supralabyrinthine space. The high resolution images showing the supralabyrinthine space suggested that the novel CBCT system is capable of detecting the cholesteatoma occurred in such insidious area in the temporal bone.

X-ray microtomography (μCT) is capable of reaching a spatial resolution of 1.7 μm, and displayed the stria vascularis, spiral ligament, Reissner's membrane, among other structures and even revealed a membrane rupture within the human cochlea (Zou et al., 2015c). Using μCT, the distribution of transtympanically injected silver nanoparticles in the middle and inner ear of the rat and their transportation pathway following injection were visualized (Zou et al., 2015d). However, it can only be used for *Ex vivo* studies due to the limited size of imaging plateform and extremely high dose of radiation (Zou et al., 2016).

Accurate 3-dimensional printing temporal bone models based on clinical CT scans was reportedly beneficial for preoperative simulation of specific challenging otologic cases in children, potentially reducing medical errors and improving patient safety (Rose et al., 2015). It is relevant to acquire images using the present novel CBCT system to reduce the X-ray dosage while guaranteeing the high resolution of images. 3-dimensional printing temporal bone might also be used for

educational temporal bone training and pre-operative training in other challenging cases (Hochman et al., 2014, 2015; Mowry et al., 2015). The CBCT data may also be used in virtual reality temporal bone training for the residents in the future (Andersen et al., 2016a, 2016b).

5. Conclusions

The novel high-resolution CBCT system was found to be powerful in the detection of the fine middle ear and inner ear structures and facial nerve pathway within the temporal bone. This system potentially has broad applications in the diagnoses of inner ear diseases, the detection of associated pathological changes, surgical planning, navigation for the ear surgery, and temporal bone training. However, the present work did not intend to provide normal values in the temporal bone due to the limited number of samples.

Declaration of conflicting interests

The authors declared no potential conflicts of interest with respect to the research, authorship, and/or publication of this article.

Funding

This work was supported by EC FP7 collaborative project NANOCI (grant agreement number: 281056) and National Natural Science Foundation of China (81170914/H1304).

References

Andersen, S.A., Mikkelsen, P.T., Konge, L., Caye-Thomasen, P., Sorensen, M.S., 2016a. Cognitive load in mastoidectomy skills training: virtual reality simulation and traditional dissection compared. J. Surg. Educ. 73, 45−50.

Andersen, S.A., Foghsgaard, S., Konge, L., Caye-Thomasen, P., Sorensen, M.S., 2016b. The effect of self-directed virtual reality simulation on dissection training performance in mastoidectomy. Laryngoscope 126, 1883−1888.

Boston, M., Halsted, M., Meinzen-Derr, J., Bean, J., Vijayasekaran, S., Arjmand, E., Choo, D., Benton, C., Greinwald, J., 2007. The large vestibular aqueduct: a new definition based on audiologic and computed tomography correlation. Otolaryngol. Head. Neck Surg. 136, 972−977.

Brantberg, K., Greitz, D., Pansell, T., 2004. Subarcuate venous malformation causing audio-vestibular symptoms similar to those in superior canal dehiscence syndrome. Otol. Neurotol. 25, 993−997.

Bremke, M., Luers, J.C., Anagiotos, A., Gostian, A.O., Dorn, F., Kabbasch, C., Unkel, C., Hollering, J., Beutner, D., 2015. Comparison of digital volume tomography and high-resolution computed tomography in detecting superior semicircular canal dehiscence−a temporal bone study. Acta Otolaryngol. 135, 901−906.

Eibenberger, K., Carey, J., Ehtiati, T., Trevino, C., Dolberg, J., Haslwanter, T., 2014. A novel method of 3D image analysis of high-resolution cone beam CT and multi slice CT for the detection of semicircular canal dehiscence. Otol. Neurotol. 35, 329−337.

Erovic, B.M., Daly, M.J., Chan, H.H., James, A.L., Papsin, B.C., Pothier, D.D., Dixon, B., Irish, J.C., 2013. Evaluation of intraoperative cone beam computed tomography and optical drill tracking in temporal bone surgery. Laryngoscope 123, 2823−2828.

Gluth, M.B., Cohen, M.A., Friedland, P.L., Atlas, M.D., 2011. Surgical anatomy of the anterior supralabyrinthine air cell tract. J. Laryngol. Otol. 125, 1009−1013.

Hochman, J.B., Kraut, J., Kazmerik, K., Unger, B.J., 2014. Generation of a 3D printed temporal bone model with internal fidelity and validation of the mechanical construct. Otolaryngol. Head. Neck Surg. 150, 448−454.

Hochman, J.B., Rhodes, C., Wong, D., Kraut, J., Pisa, J., Unger, B., 2015. Comparison of cadaveric and isomorphic three-dimensional printed models in temporal bone education. Laryngoscope 125, 2353−2357.

Husstedt, H.W., Aschendorff, A., Richter, B., Laszig, R., Schumacher, M., 2002. Nondestructive three-dimensional analysis of electrode to modiolus proximity. Otol. Neurotol. 23, 49−52.

Jiang, L.X., Xiao, Z.W., Ma, Y.K., Tu, B., Long, Z., Liao, Z.F., 2012. Combined subtemporal-supralabyrinthine approach to geniculate ganglion for management of facial paralysis in temporal bone fracture. J. Otol. 7, 31−35.

Jung, J.H., Hyun, S.M., Park, H.J., Yoon, T.H., 2013. Trans-tensor tympani facial nerve decompression in traumatic facial nerve palsy. J. Laryngol. Otol. 127, 936−938.

Komori, M., Yamada, K., Hinohira, Y., Aritomo, H., Yanagihara, N., 2013. Width of the normal facial canal measured by high-resolution cone-beam computed tomography. Acta Otolaryngol. 133, 1227−1232.

Ma, X., Yang, Y., Xia, M., Li, D., Xu, A., 2009. Computed tomography findings in large vestibular aqueduct syndrome. Acta Otolaryngol. 129, 700−708.

Minor, L.B., Solomon, D., Zinreich, J.S., Zee, D.S., 1998. Sound- and/or pressure-induced vertigo due to bone dehiscence of the superior semicircular canal. Arch. Otolaryngol. Head. Neck Surg. 124, 249−258.

Mowry, S.E., Jammal, H., Myer, C.T., Solares, C.A., Weinberger, P., 2015. A novel temporal bone simulation model using 3D printing techniques. Otol. Neurotol. 36, 1562−1565.

Murai, A., Kariya, S., Tamura, K., Doi, A., Kozakura, K., Okano, M., Nishizaki, K., 2013. The facial nerve canal in patients with Bell's palsy: an investigation by high-resolution computed tomography with multiplanar reconstruction. Eur. Arch. Otorhinolaryngol. 270, 2035−2038.

Ni, Y., Wang, K., Jiang, Y., Zhou, R., Sha, Y., Li, H., 2016. Quantitative assessment of surgical anatomy and three-dimensional relationships in the supralabyrinthine space. ORL J. Otorhinolaryngol. Relat. Spec. 78, 259−267.

Pearl, M.S., Roy, A., Limb, C.J., 2014. High-resolution secondary reconstructions with the use of flat panel CT in the clinical assessment of patients with cochlear implants. AJNR Am. J. Neuroradiol. 35, 1202−1208.

Rajati, M., Pezeshki Rad, M., Irani, S., Khorsandi, M.T., Motasaddi Zarandy, M., 2014. Accuracy of high-resolution computed tomography in locating facial nerve injury sites in temporal bone trauma. Eur. Arch. Otorhinolaryngol. 271, 2185−2189.

Rose, A.S., Webster, C.E., Harrysson, O.L., Formeister, E.J., Rawal, R.B., Iseli, C.E., 2015. Pre-operative simulation of pediatric mastoid surgery with 3D-printed temporal bone models. Int. J. Pediatr. Otorhinolaryngol. 79, 740−744.

Stutzki, M., Jahns, E., Mandapathil, M.M., Diogo, I., Werner, J.A., Guldner, C., 2015. Indications of cone beam CT in head and neck imaging. Acta Otolaryngol. 135, 1337−1343.

Verbist, B.M., Frijns, J.H., Geleijns, J., van Buchem, M.A., 2005. Multisection CT as a valuable tool in the postoperative assessment of cochlear implant patients. AJNR Am. J. Neuroradiol. 26, 424−429.

World Medical Association, Inc, 2015. WMA Declaration of Helsinki - Ethical Principles for Medical Research Involving Human Subjects. http://www.wma.net/en/30publications/10policies/b3/.

Yamakami, I., Uchino, Y., Kobayashi, E., Yamaura, A., 2003. Computed tomography evaluation of air cells in the petrous bone−relationship with postoperative cerebrospinal fluid rhinorrhea. Neurol. Med. Chir. (Tokyo) 43, 334−338 discussion 339.

Yamane, H., Konishi, K., Sakamaoto, H., Yamamoto, H., Matsushita, N., Oishi, M., Iguchi, H., Inoue, Y., 2015. Practical 3DCT imaging of the

vestibular aqueduct for Meniere's disease. Acta Otolaryngol. 135, 799−806.

Zalewski, C.K., Chien, W.W., King, K.A., Muskett, J.A., Baron, R.E., Butman, J.A., Griffith, A.J., Brewer, C.C., 2015. Vestibular dysfunction in patients with enlarged vestibular aqueduct. Otolaryngol. Head. Neck Surg. 153, 257−262.

Zhou, G., Ohlms, L., Liberman, J., Amin, M., 2007. Superior semicircular canal dehiscence in a young child: implication of developmental defect. Int. J. Pediatr. Otorhinolaryngol. 71, 1925−1928.

Zou, J., Koivisto, J., Lahelma, J., Aarnisalo, A., Wolff, J., Pyykko, I., 2015a. Imaging optimization of temporal bones with cochlear implant using a high-resolution cone beam CT and the corresponding effective dose. Ann. Otol. Rhinol. Laryngol. 124, 466−473.

Zou, J., Lahelma, J., Koivisto, J., Dhanasingh, A., Jolly, C., Aarnisalo, A., Wolff, J., Pyykko, I., 2015b. Imaging cochlear implantation with round window insertion in human temporal bones and cochlear morphological variation using high-resolution cone beam CT. Acta Otolaryngol. 135, 466−472.

Zou, J., Hannula, M., Lehto, K., Feng, H., Lahelma, J., Aula, A.S., Hyttinen, J., Pyykko, I., 2015c. X-ray microtomographic confirmation of the reliability of CBCT in identifying the scalar location of cochlear implant electrode after round window insertion. Hear Res. 326, 59−65.

Zou, J., Hannula, M., Misra, S., Feng, H., Labrador, R.H., Aula, A.S., Hyttinen, J., Pyykko, I., 2015d. Micro CT visualization of silver nanoparticles in the middle and inner ear of rat and transportation pathway after transtympanic injection. J. Nanobiotechnol. 13, 5.

Zou, J., Pyykko, I., Hyttinen, J., 2016. Inner ear barriers to nanomedicine-augmented drug delivery and imaging. J. Otol. 11 (4), 165−177.